Cation site preferences in layered oxide chalcogenides, synthesis, structures and magnetic ordering in $Sr_{3-x}Ca_xFe_2O_5Cu_2Ch_2$ (*Ch* = S, Se; *x* = 1, 2)

Bradley C. Sheath,[a] Simon J. Cassidy,[a] and Simon J. Clarke[a,*]

[a]*Department of Chemistry, University of Oxford, Inorganic Chemistry Laboratory, South Parks Road, Oxford OX1 3QR, United Kingdom*

email address: simon.clarke@chem.ox.ac.uk

Abstract

Solid solutions between the known compounds $Ca_2FeO_3Cu\mathit{Ch}$ and $Sr_2FeO_3Cu\mathit{Ch}$ (*Ch* = S, Se) in which there are two fairly similar sites (8 and 9 coordinate) for the alkaline earth cations are not attainable under standard high temperature solid state syntheses under thermodynamic control. Instead compounds with greater condensation of FeO_5 square pyramids form as these afford one 8-coordinate site and one 12-coordinate site for the alkaline earths which is better suited to the size-mismatched cations in the compounds $Sr_{3-x}Ca_xFe_2O_5Cu_2\mathit{Ch}_2$ (*Ch* = S, Se; *x* = 1, 2). $Sr_2CaFe_2O_5Cu_2S_2$, $SrCa_2Fe_2O_5Cu_2S_2$, $Sr_2CaFe_2O_5Cu_2Se_2$ and $SrCa_2Fe_2O_5Cu_2Se_2$ all crystallise in the tetragonal space group *I*4/*mmm* with two formula units in the unit cell with the crystal structure first described for $Sr_3Fe_2O_5Cu_2S_2$. Oxide slabs composed of vertex-sharing FeO_5 square pyramids are separated by $Cu_2\mathit{Ch}_2$ anti-fluorite-type layers. The larger Sr^{2+} ions have a strong preference for the 12-coordinate site in the oxide slabs, while Ca^{2+} cations dominate the 8-coordinate sites separating the oxide and chalcogenide slabs. Powder neutron diffraction reveals that all the compounds display antiferromagnetic long range ordering of the Fe^{3+} moments with ordering temperatures well above room temperature and exceeding 526 K in the case of $Ca_2SrFe_2O_5Cu_2Se_2$.

KEYWORDS: *oxychalcogenide; oxide selenide; magnetic order;*

Introduction

Mixed-anion compounds often adopt layered structures and behave electronically as two-dimensional materials. This can lead to interesting physical properties such as good thermoelectric performance [1], superconductivity[2] and complex magnetism[3-5]. In oxide sulfide and oxide selenide systems, it is the contrast in chemical nature of the two anions that drives the segregation into oxide and chalcogenide slabs, where each distinct layer can potentially host the same metal cation or different metal species[6]. These slabs can be thought of as chemical 'building blocks' [7-10] enabling the construction of novel materials, generally with alternating oxide and chalcogenide or pnictide layers. Not only can these types of compound be tuned via substitution of the constituent ions on each crystallographic site [11,12], but they can also be modified using 'soft' chemistry techniques, such as the intercalation of alkali metals between the layers [13], ion exchange [14,15], or sometimes the deintercalation of a metal ion to change the electron count [16].

When magnetic transition metal ions are present in oxychalcogenide compounds, long range magnetic ordering can arise. This is the case for the oxide sulfides Sr_2FeO_3CuS and $Sr_3Fe_2O_5Cu_2S_2$, related to the compounds described in this paper and the structures of which are displayed in Figure 1. Both Sr_2FeO_3CuS and $Sr_3Fe_2O_5Cu_2S_2$ were first discovered by Zhu and Hor in 1997 [17]. Magnetic studies on $Sr_3Fe_2O_5Cu_2S_2$ have since been carried out by Lü *et al* [18] revealing that, analogous to the $Sr_3Fe_2O_5Cu_2Se_2$ material studied by Cario *et al* [19], there is antiferromagnetic order of the Fe^{3+} ions and the moments are directed in the *ab*-plane.

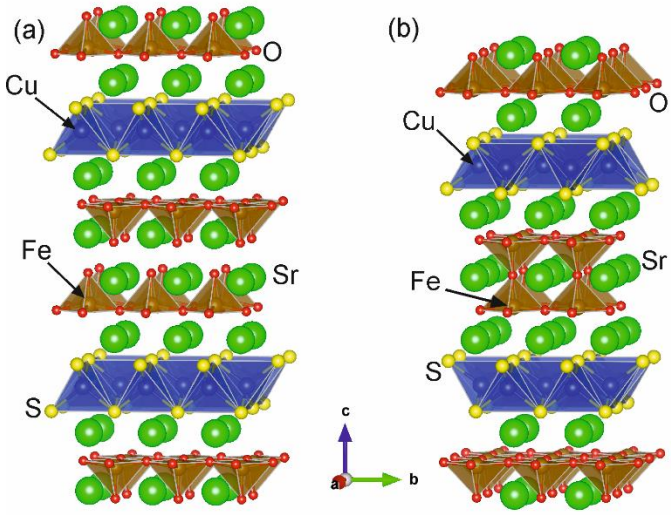

Figure 1. The crystal structures of (a) Sr_2FeO_3CuS and (b) $Sr_3Fe_2O_5Cu_2S_2$. Formally the structure of Sr_2FeO_3CuS may be derived from that of $Sr_3Fe_2O_5Cu_2S_2$ by the insertion of an SrO layer into the oxide slab [10].

Here we report the structure and magnetism of the four compounds $Sr_2CaFe_2O_5Cu_2S_2$, $SrCa_2Fe_2O_5Cu_2S_2$, $Sr_2CaFe_2O_5Cu_2Se_2$ and $SrCa_2Fe_2O_5Cu_2Se_2$, which are isostructural with $Sr_3Fe_2O_5Cu_2S_2$ and $Sr_3Fe_2O_5Cu_2Se_2$ and obtained by isovalent substitutions on the alkaline earth metal sites. These compounds were discovered when attempting the syntheses of $CaSrFeO_3CuS$ and $CaSrFeO_3CuSe$, members of the solid solution between the $Ca_2FeO_3Cu\mathit{Ch}$ [20] and $Sr_2FeO_3Cu\mathit{Ch}$ [17,21] end members. Here we rationalise the difficulty of obtaining the intended target solid solution under ambient pressure conditions and describe the magnetic ordering and structures in the attainable $Sr_{3-x}Ca_xFe_2O_5Cu_2\mathit{Ch}_2$ (*Ch* = S, Se; *x* = 1, 2) members.

Experimental

3 g samples of the four target compounds $Ca_2SrFe_2O_5Cu_2Se_2$, $CaSr_2Fe_2O_5Cu_2Se_2$, $Ca_2SrFe_2O_5Cu_2S_2$ and $CaSr_2Fe_2O_5Cu_2S_2$ were synthesised from SrO, CaO (Alfa Aesar 99.95%), CuO (Alfa Aesar 99.995%), Fe (Alfa Aesar 99.998%) and Se (Alfa Aesar 99.999%) or S (Alfa Aesar 99.999%) under an inert argon atmosphere. SrO had been previously prepared via thermal decomposition of $SrCO_3$ (Alfa Aesar 99.994%) by heating it at 830°C for 16 hours and then 1100°C for 4 hours, all under dynamic vacuum. Stoichiometric mixtures of the reactants were ground together using an agate pestle and mortar until homogeneous. The batch was then split and two approximately 1.5 g pellets were pressed in a 13 mm pellet die under 3-4 tonnes of force. Both pellets were sealed inside a silica tube under vacuum. The selenides were heated at 675°C for 36h then at 900°C for 60h, whereas the sulfides were heated at 400°C for 36h then at 900°C for 60h. The preliminary lower temperature heating steps were used to ensure that the volatile chalcogenides reacted without attaining high vapour pressures. Grinding and re-pelletising was performed between the two heating steps. This two-step heating cycle was found to be adequate for very high purity samples. It should be noted that similar synthetic routes were used when initially attempting the syntheses of the $CaSrFeO_3CuSe$ and $CaSrFeO_3CuS$ target compounds (with the structure shown in Figure 1(a)).

X-ray powder diffraction (XRPD) data to follow the reactions were performed on a Bruker D8 Advance Eco diffractometer using Cu Kα radiation. Data for detailed structural analysis were collected on beamline I11 [22] at the Diamond Light Source using 30 minute scans with 0.82 Å X-rays (calibrated using a Si standard) with the high resolution Multi-Analyser Crystal (MAC) detector. The Position Sensitive Detector (PSD) was also used on beamline I11 [22] to gather data at approximately

160 temperatures between 300 K and 700 K. Neutron powder diffraction (NPD) was carried out on the WISH instrument [23] at the ISIS Facility, where approximately 2 g of each material was loaded into vanadium cans and the neutron scattering data were obtained at various temperatures between 1.5 K and 570 K using a cryofurnace to cool down and warm up the samples. The XRPD and NPD data were analysed by Rietveld refinement using the TOPAS Academic V5 software [24].

Results and Discussion

Compositions and Crystal Structures

While the compounds $Ca_2FeO_3Cu\mathit{Ch}$ [20] and $Sr_2FeO_3Cu\mathit{Ch}$ [17,21] have been reported (structure in Figure 1(a)), attempts to synthesise members of the solid solutions $Sr_{2-x}Ca_xFeO_3CuS$ and $Sr_{2-x}Ca_xFeO_3CuSe$ invariably resulted in products isostructural with the related compound $Sr_3Fe_2O_5Cu_2S_2$ (structure in Figure 1(b)) together with excess unreacted alkaline earth oxide. We therefore subsequently targeted the phases with the $Sr_3Fe_2O_5Cu_2S_2$ structure: $Ca_2SrFe_2O_5Cu_2Se_2$, $CaSr_2Fe_2O_5Cu_2Se_2$, $Ca_2SrFe_2O_5Cu_2S_2$ and $CaSr_2Fe_2O_5Cu_2S_2$ as described in the experimental section. These products were all attainable with negligible contamination by side phases according to the results of XRPD measurements.

All the products were found to crystallise in the *I*4/*mmm* space group, confirming that they adopt the undistorted $Sr_3Fe_2O_5Cu_2S_2$ structure (Figure 1(b)). The refinements against XRPD (Figure 2) and NPD (Figure 3) data for $Ca_2SrFe_2O_5Cu_2Se_2$ are shown below and the refinements for the other compounds are shown in the supporting information (Figures S1-S3). These layered materials comprise $[\mathit{Ae}Fe_2O_5]^{2-}$ slabs (*Ae* = alkaline earth) containing Fe^{3+} cations in double layers of all-vertex-linked FeO_5 square pyramids separated by anti-PbO-type $[Cu_2\mathit{Ch}_2]^{2-}$ layers, where Cu^+ cations are surrounded by chalcogenide anions in a tetrahedral arrangement. Two distinct alkaline earth metal sites are positioned within the oxide slabs (12-coordinate by oxide ions) and between these and the chalcogenide layers (8-coordinate by 4 oxide and 4 chalcogenide ions). Figure 4(a) depicts this structure.

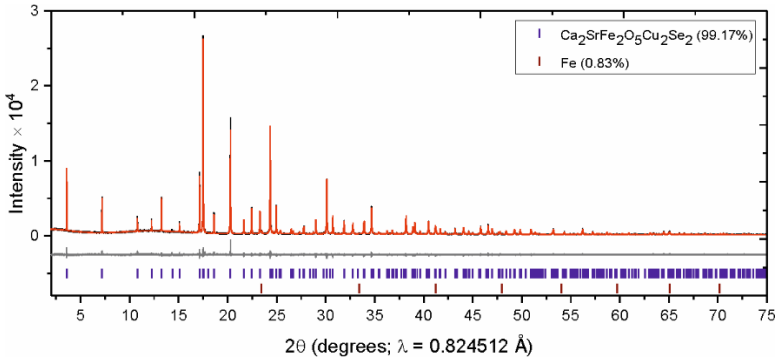

Figure 2. XRPD pattern of $Ca_2SrFe_2O_5Cu_2Se_2$ measured at 300 K on the MAC detector at I11 showing the observed (black), calculated (red) and difference (grey) curves. R_{wp}: 7.625%.

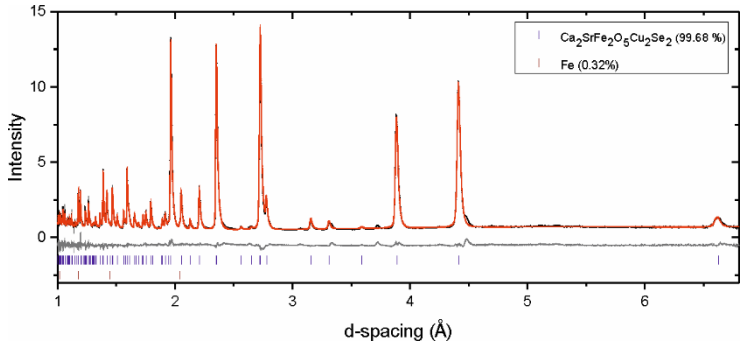

Figure 3. NPD pattern of $Ca_2SrFe_2O_5Cu_2Se_2$ (combination of banks 3 and 8 with average $2\theta = 90°$) measured at 568 K on the WISH instrument at ISIS showing the observed (black), calculated (red) and difference (grey) curves. R_{wp}: 3.942%.

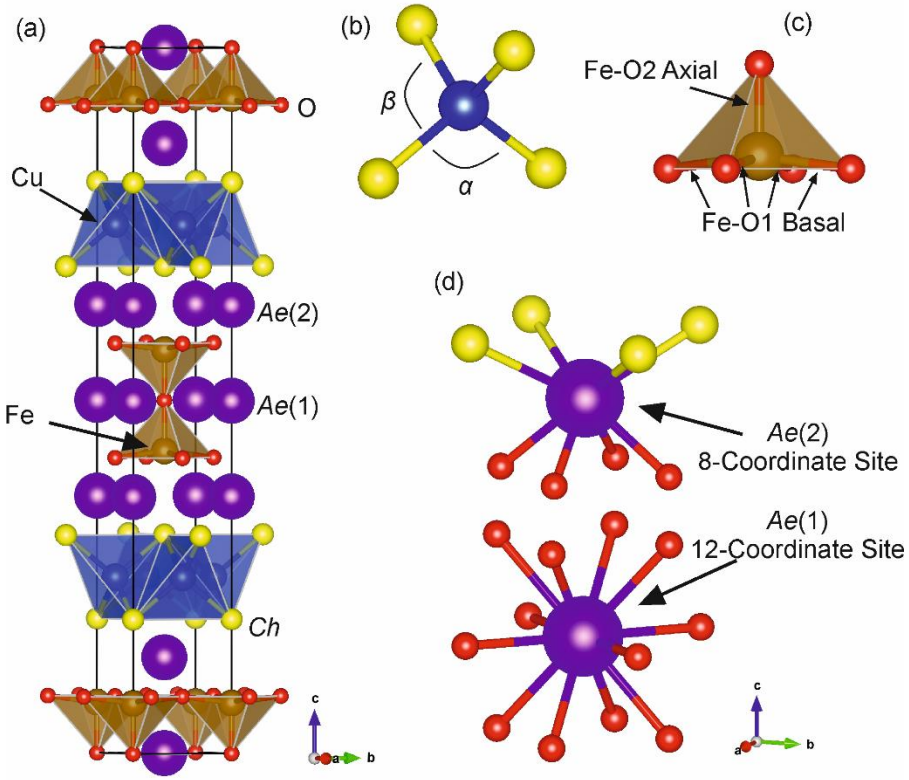

Figure 4. (a) The structure of the $Sr_{3-x}Ca_xFe_2O_5Cu_2Ch_2$ (*Ch* = S, Se; *x* = 1, 2) compounds. **(b)** The *α* and *β* angles in the copper chalcogenide tetrahedra. **(c)** The Fe-O1 basal and Fe-O2 axial bonds in the iron oxide square-based pyramids. **(d)** A detailed view of the coordination of the *Ae*(1) and *Ae*(2) alkaline earth metal sites.

Structure refinement

The refined lattice parameters and selected bond lengths and angles are displayed in Table 1. A comparison between the XRPD and NPD refined atomic positions for $Ca_2SrFe_2O_5Cu_2Se_2$ (Table S1) and the base temperature NPD refinements for all four compounds (Table S3) are shown in the supporting information. There is an increase in lattice parameters with the introduction of ions with larger ionic radii, such as when Ca^{2+} cations are substituted by Sr^{2+} cations or when the chalcogenide ions present are selenide anions rather than sulfide anions. The FeO_5 square-based pyramids have larger basal Fe-O1 bonds but shorter axial Fe-O2 bonds in the selenides compared with the sulfides. This apparent compression of the $[Fe_2O_5]^{4-}$ layers is probably due to the expansion of the $[Cu_2Ch_2]^{2-}$ layers upon going from the sulfides to the selenides. The simultaneous expansion of the basal Fe-O1 bonds and compression of the axial Fe-O2 bonds ensures that the bond valence sum of the Fe ions remains approximately constant, satisfying the bonding requirements of the metal cation.

	$Ca_2SrFe_2O_5Cu_2Se_2$	**$CaSr_2Fe_2O_5Cu_2Se_2$**	**$Ca_2SrFe_2O_5Cu_2S_2$**	**$CaSr_2Fe_2O_5Cu_2S_2$**
Space Group	*I*4/*mmm* (No 139)	*I*4/*mmm* (No 139)	*I*4/*mmm* (No 139)	*I*4/*mmm* (No 139)
R_{wp} (%)	7.570	8.968	7.112	6.413
χ^2	3.914	5.100	3.447	4.420
a (Å)	3.913980(8)	3.93683(2)	3.880589(15)	3.902499(17)
c (Å)	26.34765(9)	26.6536(2)	25.60252(14)	25.96073(15)
V (Å^3)	403.626(2)	413.093(5)	385.548(4)	395.369(4)
Fe-*Ch* (Å) [1][a]	3.1280(8)	3.2246(10)	3.0518(10)	3.1571(10)
Cu-*Ch* (Å) [4] [a]	2.5086(3)	2.5118(4)	2.4243(5)	2.4288(5)
Fe-O1 (Å) [4] [a]	1.9728(3)	1.9844(4)	1.9573(3)	1.96814(19)
Fe-O2 (Å) [1] [a]	1.8894(6)	1.8785(9)	1.8954(6)	1.8868(6)
Ch-Cu-*Ch* α (°) [2] [a]	102.540(17)	103.19(2)	106.33(3)	106.91(3)
Ch-Cu-*Ch* β (°) [4] [a]	113.044(9)	112.698(11)	111.066(15)	110.768 (16)
O1-Fe-O2 (°) [4] [a]	97.27(6)	97.27(8)	97.57(5)	97.51(5)
Fe BV Sum	2.947(3)	2.899(4)	3.032(3)	2.981(2)

[a] Numbers in square brackets indicate the number of bonds or angles of each type.

Table 1. Refinement results from XRPD patterns collected at 300 K using the MAC detector at I11. The specific Fe-O bonds and *Ch*-Cu-*Ch* bond angles are defined in Figures 4(b) and 4(c). Bond valence calculations were performed using literature data from Brown and Altermatt [25] in tandem with values in this table.

Cation ordering

The site preferences of the Ca^{2+} and Sr^{2+} cations was explored by refining their occupancies on the two available alkaline earth metal sites, *Ae*(1) in the centre of the oxide slabs and *Ae*(2) between the oxide and chalcogenide slabs. A single parameter was refined and the refinement was constrained such that the Ca:Sr ratio was fixed according to the composition of the synthesis and both sites were assumed to be fully occupied. The X-ray data was used for this analysis due to the absence of the magnetic Bragg peaks and the higher scattering contrast between Sr and Ca for X-ray diffraction compared with neutron diffraction. *Ae*(1) is the larger crystallographic site with a coordination number of 12 (12 × O) forming a cuboctahedron whereas *Ae*(2) is the smaller site with a coordination number of 8 (4 × O and 4 × *Ch*) forming a distorted square antiprism (see Figure 4(d)). The refined occupancies derived from the synchrotron XRPD data are given in Table 2 (results from the low temperature NPD data are included in Table S2) and a visual representation displayed in Figure 5. It is clear from the data that the Sr^{2+} cations preferentially fill the larger *Ae*(1) site and the Ca^{2+} cations tend to occupy the *Ae*(2) position. The most likely reasoning behind this cation ordering is that the larger Sr^{2+} cation forces the smaller Ca^{2+} cation onto the smaller crystallographic site. When there are more Sr^{2+} cations than there are *Ae*(1) sites, as in the case of $CaSr_2Fe_2O_5Cu_2Se_2$ and $CaSr_2Fe_2O_5Cu_2S_2$, this larger site is indeed almost completely filled by Sr^{2+} cations, whereas when the ions are in the same ratio as the sites, as in the case of $Ca_2SrFe_2O_5Cu_2Se_2$ and $Ca_2SrFe_2O_5Cu_2S_2$, the segregation is not quite complete and there is significant antisite disorder in $Ca_2SrFe_2O_5Cu_2Se_2$ and $Ca_2SrFe_2O_5Cu_2S_2$: about 8-10% of the more abundant Ca^{2+} ions are not on the *Ae*(2) site and 16-20% of the Sr^{2+} ions are not on their preferred *Ae*(1) site. Whether this can be reduced by changing the synthesis temperature or pressure has not been explored in this work. The nature of the chalcogenide has relatively little effect on the degree of antisite disorder.

Table 2. Site preferences for Sr^{2+} and Ca^{2+} cations on the *Ae*(1) and *Ae*(2) crystallographic sites.

	***Ae*(1) Occupancy (Larger Site)**	***Ae*(2) Occupancy (Smaller Site)**
$Ca_2SrFe_2O_5Cu_2Se_2$	Sr 0.836(2) Ca 0.164(2)	Sr 0.082(1) Ca 0.918(1)
$CaSr_2Fe_2O_5Cu_2Se_2$	Sr 0.972(3) Ca 0.028(3)	Sr 0.514(1) Ca 0.486(1)
$Ca_2SrFe_2O_5Cu_2S_2$	Sr 0.795(2) Ca 0.205(2)	Sr 0.103(1) Ca 0.897(1)
$CaSr_2Fe_2O_5Cu_2S_2$	Sr 0.970(2) Ca 0.030(2)	Sr 0.515(1) Ca 0.485(1)

Refined using data collected at 300 K on the MAC detector at I11.

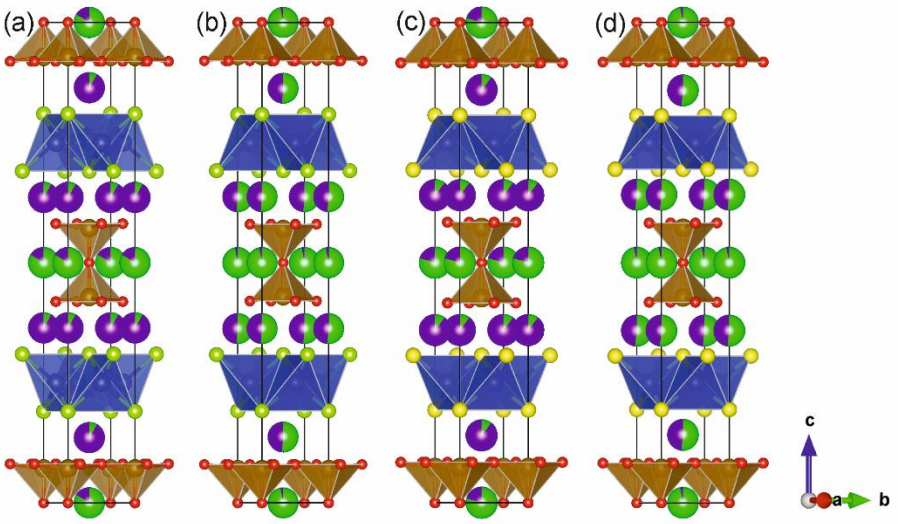

Figure 5. The fractional occupancies of the alkaline earth metal sites by Ca^{2+} (purple) and Sr^{2+} (green) of **(a)** $Ca_2SrFe_2O_5Cu_2Se_2$ **(b)** $CaSr_2Fe_2O_5Cu_2Se_2$ **(c)** $Ca_2SrFe_2O_5Cu_2S_2$ and **(d)** $CaSr_2Fe_2O_5Cu_2S_2$.

It is the inclusion of alkaline earth metal cations with varying ionic radii which appears to force the target compounds in the proposed solid solution $Sr_{2-x}Ca_xFeO_3Cu\mathit{Ch}$ with the $\mathit{Ae}_2\mathit{M}O_3Cu\mathit{Ch}$ structure in space group *P*4/*nmm* (Figure 1(a)) to produce instead compounds adopting the $\mathit{Ae}_3\mathit{M}_2O_5Cu_2\mathit{Ch}_2$ structure in space group *I*4/*mmm* (Figure 1(b)), with the expulsion of excess alkaline earth oxide. The $\mathit{Ae}_3\mathit{M}_2O_5Cu_2\mathit{Ch}_2$ structure in space group *I*4/*mmm* contains two alkaline earth metal sites of contrasting sizes, which are able to host the Sr^{2+} and Ca^{2+} cations in a seemingly more energetically favourable manner. The $\mathit{Ae}_2\mathit{M}O_3Cu\mathit{Ch}$ structure in space group *P*4/*nmm* however contains two relatively similar alkaline earth metal sites. So while $Ca_2FeO_3Cu\mathit{Ch}$ and $Sr_2FeO_3Cu\mathit{Ch}$ (*Ch* = S, Se) are both known to crystallise in the $\mathit{Ae}_2\mathit{M}O_3Cu\mathit{Ch}$ structure in *P*4/*nmm*, when solid solutions between these end members are attempted, the result is the formation of compounds $Sr_{3-x}Ca_xFe_2O_5Cu_2\mathit{Ch}_2$ (*Ch* = S, Se; *x* = 1, 2) which crystallise in the $\mathit{Ae}_3\mathit{M}_2O_5Cu_2\mathit{Ch}_2$ structure in *I*4/*mmm* together with excess *Ae*O.

Magnetic ordering

NPD data collected at ambient temperatures showed the presence of additional reflections at longer *d*-spacings that were consistent with an ordering of Fe^{3+} moments on a cell which was a $\sqrt{2}a_{nuc} \times \sqrt{2}a_{nuc} \times c_{nuc}$ expansion of the nuclear unit cell. These magnetic reflections became more intense at lower temperatures (see Figure S4) and have been highlighted in the NPD data shown in Figure 6 for $Ca_2SrFe_2O_5Cu_2Se_2$. The data and refinements at low temperatures for the other phases are presented in the supporting information (Figures S7-S9). Analysis of the intensities of these magnetic Bragg peaks using ISODISTORT [26] and Rietveld refinement was carried out

systematically by first assessing individual magnetic modes and then combinations of two modes operating simultaneously. This resulted in a model for the long range magnetic ordering which could be described using a combination of two antiferromagnetically ordered magnetic modes, both with propagation vector $k = (1/2\ 1/2\ 0)$. These modes are denoted as mX1- A2(a,0) and mX3- E(a,0), which align the Fe^{3+} moments along the *c*-axis and in the *ab*-plane respectively. Therefore the model, shown in Figure 7, has the Fe^{3+} moments tilted away from the crystallographic axes. It should be noted that this model is the simplest one that accounts for the magnetic intensities in the NPD data. Due to the limitation on defining the moment directions in the *ab*-plane for a tetragonal system using powder data [27], it is plausible that alternative models where the components of the moment in the *ab*-plane are non-collinear may account for the observed magnetic intensities. It may be possible to gain further information on this from single crystal neutron scattering measurements, which would also enable the spin-dynamics and strengths of the exchange interactions, together with the critical behaviour around T_N, to be elucidated further.

Refinement results for the four compounds at base temperature are given in Table 3. All four compounds can be described using the same magnetic model and contain Fe^{3+} magnetic moments of comparable direction and magnitude. The large moment reduction from the free-ion value of 5 μ_B for high spin d^5 Fe^{3+} due to the covalent interaction with the oxide ions is typical for transition metal oxides. However, the sulfides have smaller saturated long range ordered magnetic moments at low temperatures than the selenides. Figure 8 shows how the base temperature magnetic moment increases as the Fe bond valence sum decreases. Presumably the higher Fe bond valence sum (shorter Fe-O distances) in the sulfides leads to a greater degree of covalency in these bonds, hence the localised ordered moment on the Fe^{3+} ions decreases. $Sr_3Fe_2O_5Cu_2Se_2$ [19] fits this trend, as it has the lowest Fe bond valence sum (longest Fe-O distances) and the largest magnetic moment.

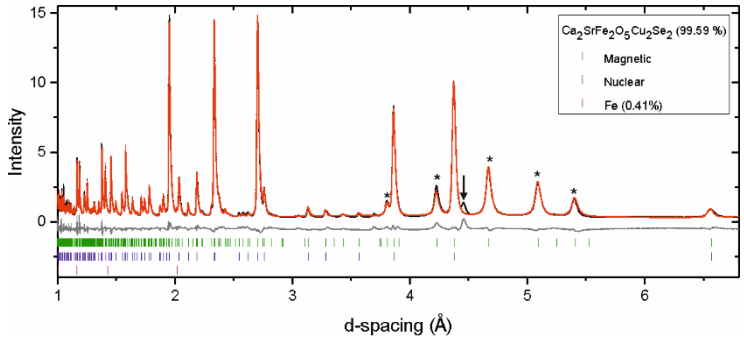

Figure 6. NPD pattern of $Ca_2SrFe_2O_5Cu_2Se_2$ (combination of banks 3 and 8 with average 2θ = 90°) measured at 5.7 K on the WISH instrument at ISIS showing the observed (black), calculated (red) and difference (grey) curves. Each * denotes a magnetic Bragg peak. The arrow denotes an impurity peak at 4.5 Å of unknown nuclear and/or magnetic origin (evident at high temperatures with similar intensity – see Figure 3). R_{wp}: 5.197%.

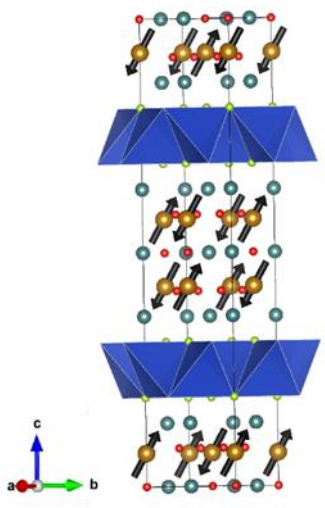

Figure 7. Model for the magnetic order in $Ca_2SrFe_2O_5Cu_2Se_2$, refined using data collected on the WISH instrument at ISIS.

Sample	Temperature (K)	Magnetic Moment (μ_B)[a]	Tilt Angle from ab-plane (degrees)	Mean Fe-O Distance [at 300 K] (Å)[b]
$Ca_2SrFe_2O_5Cu_2Se_2$	5.7	3.433(15)	58.6(3)	1.9561(4)
$CaSr_2Fe_2O_5Cu_2Se_2$	5.6	3.376(14)	57.7(3)	1.9632(5)
$Ca_2SrFe_2O_5Cu_2S_2$	5	2.930(16)	57.5(3)	1.9449(4)
$CaSr_2Fe_2O_5Cu_2S_2$	1.5	3.068(20)	58.8(4)	1.9519(3)
$Sr_3Fe_2O_5Cu_2Se_2$ [19]	2	3.6(2)	0	1.9706(18)

Table 3. Total magnetic moments and tilt angles for $Sr_{3-x}Ca_xFe_2O_5Cu_2Ch_2$ (*Ch* = S, Se; *x* = 1, 2).

[a] refined using NPD patterns obtained on the WISH instrument at ISIS.
[b] Calculated using the bond distances in Table 1.

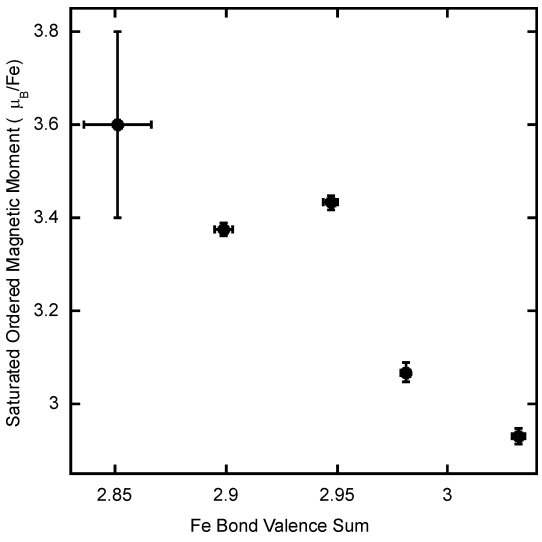

Figure 8. Correlation between the bond valence sum of Fe at 300 K and the magnetic moment at base temperature for the compounds in Table 3. The data for $Sr_3Fe_2O_5Cu_2Se_2$ are given by *Cario et al* [19].

Figure 9(a) shows the evolution of the magnetic moment in $Ca_2SrFe_2O_5Cu_2Se_2$ from the saturation value of 3.50 μ_B at low temperatures. From these data we infer a Néel temperature (T_N) of 560(5) K. The critical exponent, β, describing the behaviour of the magnitude of the ordered moment as T_N is approached, was calculated for these data (Figure S10), giving an estimated value of 0.29(2). This is consistent with a three-dimensional lattice, however closer investigation of the behaviour in the critical region close to T_N would be necessary to evaluate the spin dimensionality in this compound. Figure 9(b) reveals that a subtle spin reorientation occurs for this compound with the moment tilting slightly towards the *c*-axis as temperature increases. Measurement of the X-ray diffraction pattern for this compound between 300 K and 700 K does not reveal any structural anomaly associated with the spin-reorientation or the onset of long range magnetic ordering (Figures S5 and S6).

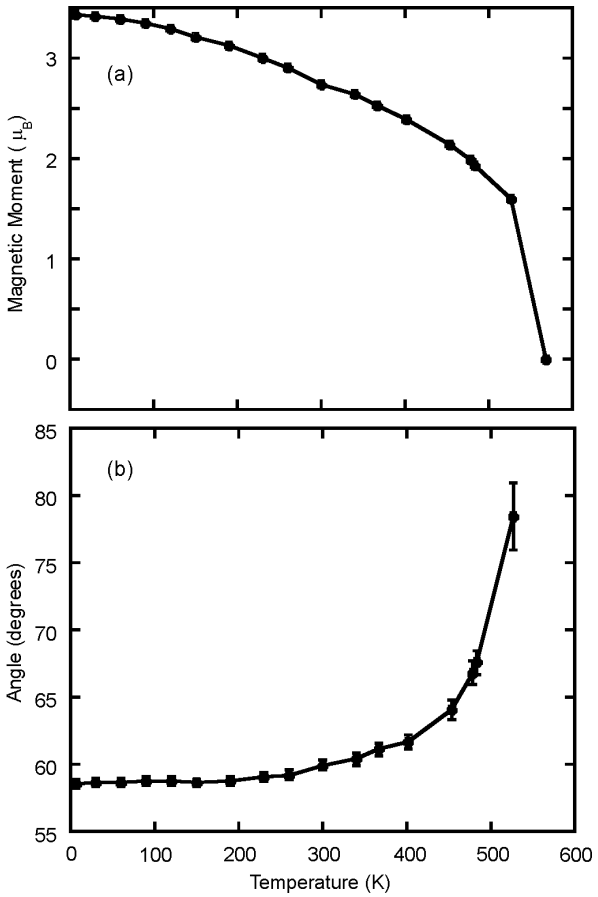

Figure 9. Thermal evolution of (a) the ordered Fe magnetic moment of $Ca_2SrFe_2O_5Cu_2Se_2$ and (b) he tilt angle (from the *ab*-plane) of the magnetic moments in $Ca_2SrFe_2O_5Cu_2Se_2$. Although the

uncertainty on the refined moment increases as the moment becomes smaller on warming, the spin reorientation appears to be significant.

Conclusions

The novel compounds $Ca_2SrFe_2O_5Cu_2Se_2$, $CaSr_2Fe_2O_5Cu_2Se_2$, $Ca_2SrFe_2O_5Cu_2S_2$ and $CaSr_2Fe_2O_5Cu_2S_2$ have been synthesised as high purity phases. In these materials, the larger Sr^{2+} cations preferentially fill the larger alkaline earth metal sites in the oxide slabs, forcing the smaller Ca^{2+} cations onto the smaller alkaline earth metal sites between the oxide and chalcogenide slabs. These compounds with two different alkaline earth metal sites are preferred when alkaline earth ions of different sizes are both present, and we were unable to prepare members of the solid solution between Ca_2FeO_3Cu*Ch* and Sr_2FeO_3Cu*Ch* because their structure does not accommodate well cations of different sizes compared with the structure of the title compounds. As Charkin *et al* [20] reported that they were unable to synthesise the isostructural $Ca_3Fe_2O_5Cu_2Ch_2$ (*Ch* = S, Se) targets using similar high temperature syntheses, this suggests that the presence of the large 12-coordinate site in the oxide layer in this structure does not readily accommodate the small Ca^{2+} cation. The inclusion of the Ca^{2+} cation in these $Sr_{3-x}Ca_xFe_2O_5Cu_2Ch_2$ (*Ch* = S, Se; *x* = 1, 2) compounds is of interest because of its lack of appearance in existing layered oxychalcogenide materials and its potential effect on the physical properties of these systems through tuning bond lengths and angles.

The magnetic structure of these materials has a cell which is a $\sqrt{2}a_{nuc} \times \sqrt{2}a_{nuc} \times c_{nuc}$ expansion of the nuclear unit cell. It consists of antiferromagnetically ordered, tilted Fe^{3+} moments which- for the case of $Ca_2SrFe_2O_5Cu_2Se_2$- reorientate towards the *c*-axis upon heating from base temperature. These materials exhibit a value for the magnetic moment per Fe^{3+} ion of less than 5 μ_B due to the presence of covalency in the Fe-O bonds. As the $Sr_3Fe_2O_5Cu_2Ch_2$ (*Ch*=Se, S) compounds have been reported to contain antiferromagnetically ordered Fe^{3+} moments directed in the *ab*-plane, these new materials show how changing the alkaline earth metal cation can tune the nature of the long range magnetic order within solids.

Acknowledgements.

We thank: the UK EPSRC (EP/M020517/1, EP/R042594/1 and EP/P018874/1) for funding and for studentship support to BCS; the ISIS pulsed neutron and muon source (RB1910207) and the Diamond Light Source Ltd (EE18786) for the award of beam time. We thank Dr. P Manuel and Dr. F Orlandi for support on WISH and Dr A. Baker and Dr C. Murray for support on I11.

Additional Information.

Supplementary information accompanies this paper at http://

Competing Interests.

The authors declare no competing interests.

Materials and Correspondence.

Correspondence and reasonable material requests should be addressed to S J Clarke (simon.clarke@chem.ox.ac.uk).

Author Information.

B. C. S. synthesised the samples. B. C. S. analysed the XRPD data that had been collected by S. J. Cassidy. B. C. S. and S. J. Cassidy collected and analysed the NPD data. B. C. S. wrote the paper with input from the other authors. S. J. Clarke provided materials and initial concepts.

References.

[1] S.D.N. Luu, P. Vaqueiro, Layered oxychalcogenides: Structural chemistry and thermoelectric properties, J. Mater. 2 (2016) 131–140. https://doi.org/10.1016/j.jmat.2016.04.002.

[2] Y. Kamihara, T. Watanabe, M. Hirano, H. Hosono, Iron-based layered superconductor La[$O_{1-x}F_x$]FeAs (x = 0.05-0.12) with T_c = 26 K, J. Am. Chem. Soc. 130 (2008) 3296–3297. https://doi.org/10.1021/ja800073m.

[3] S.J. Cassidy, M. Batuk, D. Batuk, J. Hadermann, D.N. Woodruff, A.L. Thompson, S.J. Clarke, Complex Microstructure and Magnetism in Polymorphic CaFeSeO, Inorg. Chem. 55 (2016) 10714–10726. https://doi.org/10.1021/acs.inorgchem.6b01951.

[4] H. Kabbour, E. Janod, B. Corraze, M. Danot, C. Lee, M.H. Whangbo, L. Cario, Structure and magnetic properties of oxychalcogenides $A_2F_2Fe_2OQ_2$ (A = Sr, Ba; Q = S, Se) with Fe_2O square planar layers representing an antiferromagnetic checkerboard spin lattice, J. Am. Chem. Soc. 130 (2008) 8261–8270. https://doi.org/10.1021/ja711139g.

[5] S. Skiadopoulou, M. Retuerto, F. Borodavka, C. Kadlec, F. Kadlec, M. Míšek, J. Prokleška, Z. Deng, X. Tan, C. Frank, J.A. Alonso, M.T. Fernandez-Diaz, M. Croft, F. Orlandi, P. Manuel, E. McCabe, D. Legut, M. Greenblatt, S. Kamba, Structural, magnetic, and spin dynamical properties of the polar antiferromagnets $Ni_{3-x}Co_xTeO_6$ (x = 1,2), Phys. Rev. B. 101 (2020) 14429. https://doi.org/10.1103/PhysRevB.101.014429.

[6] M. Valldor, Anion ordering in bichalcogenides, Inorganics. 4 (2016) 23. https://doi.org/10.3390/inorganics4030023.

[7] L. Cario, H. Kabbour, A. Meerschaut, Designing new inorganic compounds from 2D building blocks, Chem. Mater. 17 (2005) 234–236. https://doi.org/10.1021/cm048180p.

[8] C. Stock, E.E. McCabe, The magnetic and electronic properties of oxyselenides - Influence of transition metal ions and lanthanides, J. Phys. Condens. Matter. 28 (2016). https://doi.org/10.1088/0953-8984/28/45/453001.

[9] M.A. Hayward, Synthesis and Magnetism of Extended Solids Containing Transition-Metal Cations in Square-Planar, MO_4 Coordination Sites, Inorg. Chem. 58 (2019) 11961–11970. https://doi.org/10.1021/acs.inorgchem.9b00960.

[10] S.J. Clarke, P. Adamson, S.J.C. Herkelrath, O.J. Rutt, D.R. Parker, M.J. Pitcher, C.F. Smura, Structures, physical properties, and chemistry of layered oxychalcogenides and oxypnictides, Inorg. Chem. 47 (2008) 8473–8486. https://doi.org/10.1021/ic8009964.

[11] S. Okada, Y. Kamihara, N. Ohkubo, S. Ban, M. Matoba, Transport properties of The layered transition metal oxypnictide Sr_2ScMPO_3 with MP layers (M =Mn, Ni and $Co_{0.5}Fe_{0.5}$), J. Phys. Conf. Ser., 568 (2014) 022034. https://doi.org/10.1088/1742-6596/568/2/022034.

[12] D.G. Free, N.D. Withers, P.J. Hickey, J.S.O. Evans, Synthesis, structure and properties of several new oxychalcogenide materials with the general formula $A_2O_2M_2OSe_2$ (A = La-Sm, M = Fe, Mn), Chem. Mater. 23 (2011) 1625–1635. https://doi.org/10.1021/cm1035453.

[13] O.J. Rutt, T.L. Hill, Z.A. Gál, M.A. Hayward, S.J. Clarke, The Cation-Deficient Ruddlesden-Popper Oxysulfide $Y_2Ti_2O_5S_2$ as a Layered Sulfide: Topotactic Potassium Intercalation to Form $KY_2Ti_2O_5S_2$, Inorg. Chem. 42 (2003) 7906–7911. https://doi.org/10.1021/ic0301730.

[14] O.J. Rutt, G.R. Williams, S.J. Clarke, Reversible lithium insertion and copper extrusion in layered oxysulfides, Chem. Commun. (2006) 2869–2871. https://doi.org/10.1039/b605105g.

[15] S. Indris, J. Cabana, O.J. Rutt, S.J. Clarke, C.P. Grey, Layered oxysulfides $Sr_2MnO_2Cu_{2m-0.5}S_{m+1}$ (m = 1, 2, and 3) as insertion hosts for Li ion batteries, J. Am. Chem. Soc. 128 (2006) 13354–13355. https://doi.org/10.1021/ja064961a.

[16] J.N. Blandy, A.M. Abakumov, K.E. Christensen, J. Hadermann, P. Adamson, S.J. Cassidy, S. Ramos, D.G. Free, H. Cohen, D.N. Woodruff, A.L. Thompson, S.J. Clarke, Soft chemical control of the crystal and magnetic structure of a layered mixed valent manganite oxide sulfide, APL Mater. 3 (2015) 41520. https://doi.org/10.1063/1.4918973.

[17] W.J. Zhu, P.H. Hor, Crystal Structure of New Layered Oxysulfides: $Sr_3Cu_2Fe_2O_5S_2$ and Sr_2CuMO_3S (M=Cr, Fe, In), J. Solid State Chem. 134 (1997) 128–131. https://doi.org/10.1006/jssc.1997.7556.

[18] M. Lü, O. Mentré, E.E. Gordon, M.H. Whangbo, A. Wattiaux, M. Duttine, N. Tiercelin, H. Kabbour, A comprehensive study of magnetic exchanges in the layered oxychalcogenides $Sr_3Fe_2O_5Cu_2Q_2$ (Q = S, Se), J. Magn. Magn. Mater. 444 (2017) 147–153. https://doi.org/10.1016/j.jmmm.2017.07.026.

[19] L. Cario, A. Lafond, T. Morvan, H. Kabbour, G. André, P. Palvadeau, Design and magnetic properties of new compounds containing iron 2D building blocks of the perovskite type, Solid State Sci. 7 (2005) 936–944. https://doi.org/10.1016/j.solidstatesciences.2005.04.016.

[20] D.O. Charkin, A. V. Sadakov, O.E. Omel'Yanovskii, S.M. Kazakov, Synthesis, crystal structure, and properties of novel perovskite oxychalcogenides, Ca_2CuFeO_3Ch (Ch = S, Se), Mater. Res. Bull. 45 (2010) 2012–2016. https://doi.org/10.1016/j.materresbull.2010.07.023.

[21] D. Berthebaud, O.I. Lebedev, D. Pelloquin, A. Maignan, Structural, magnetic and transport properties of 2D structured perovskite oxychalcogenides, Solid State Sci. 36 (2014) 94–100. https://doi.org/10.1016/j.solidstatesciences.2014.08.001.

[22] S.P. Thompson, J.E. Parker, J. Potter, T.P. Hill, A. Birt, T.M. Cobb, F. Yuan, C.C. Tang, Beamline I11 at Diamond: A new instrument for high resolution powder diffraction, Rev. Sci. Instrum. 80 (2009) 879. https://doi.org/10.1063/1.3167217.

[23] L.C. Chapon, P. Manuel, P.G. Radaelli, C. Benson, L. Perrott, S. Ansell, N.J. Rhodes, D. Raspino, D. Duxbury, E. Spill, J. Norris, WISH: The new powder and single crystal magnetic diffractometer on the second target station, Neutron News. 22 (2011) 22–25. https://doi.org/10.1080/10448632.2011.569650.

[24] A.A. Coelho, TOPAS and TOPAS-Academic: An optimization program integrating computer algebra and crystallographic objects written in C++, J. Appl. Crystallogr. 51 (2018) 210–218. https://doi.org/10.1107/S1600576718000183.

[25] I.D. Brown, D. Altermatt, Bond-valence parameters obtained from a systematic analysis of the Inorganic Crystal Structure Database, Acta Crystallogr. Sect. B. 41 (1985) 244–247. https://doi.org/10.1107/S0108768185002063.

[26] B.J. Campbell, H.T. Stokes, D.E. Tanner, D.M. Hatch, ISODISPLACE: A web-based tool for exploring structural distortions, J. Appl. Crystallogr. 39 (2006) 607–614. https://doi.org/10.1107/S0021889806014075.

[27] G. Shirane, A note on the magnetic intensities of powder neutron diffraction, Acta Crystallogr. 12 (1959) 282–285. https://doi.org/10.1107/s0365110x59000871.

Cation site preferences in layered oxide chalcogenides, synthesis, structures and magnetic ordering in $Sr_{3-x}Ca_xFe_2O_5Cu_2Ch_2$ (*Ch* = S, Se; *x* = 1, 2)

Bradley C. Sheath,[a] Simon J. Cassidy,[a] and Simon J. Clarke[a,*]

[a]*Department of Chemistry, University of Oxford, Inorganic Chemistry Laboratory, South Parks Road, Oxford OX1 3QR, United Kingdom*

Supporting Information

email address: simon.clarke@chem.ox.ac.uk

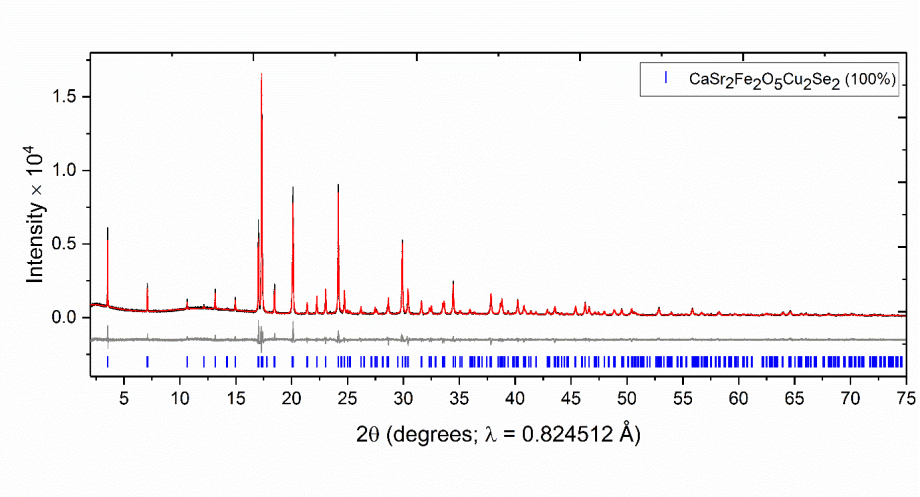

Figure S1. XRPD pattern of $CaSr_2Fe_2O_5Cu_2Se_2$ measured at 300 K on the MAC detector at I11 showing the observed (black), calculated (red) and difference (grey) curves. R_{wp}: 8.968%.

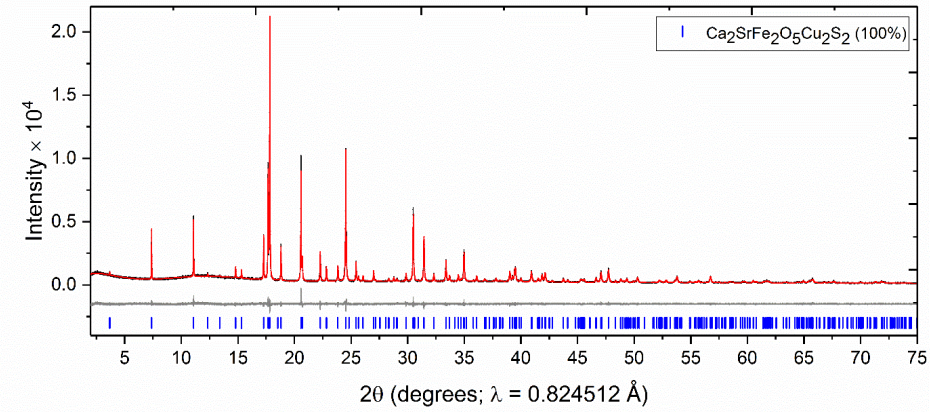

Figure S2. XRPD pattern of $Ca_2SrFe_2O_5Cu_2S_2$ measured at 300 K on the MAC detector at I11 showing the observed (black), calculated (red) and difference (grey) curves. R_{wp}: 7.112%.

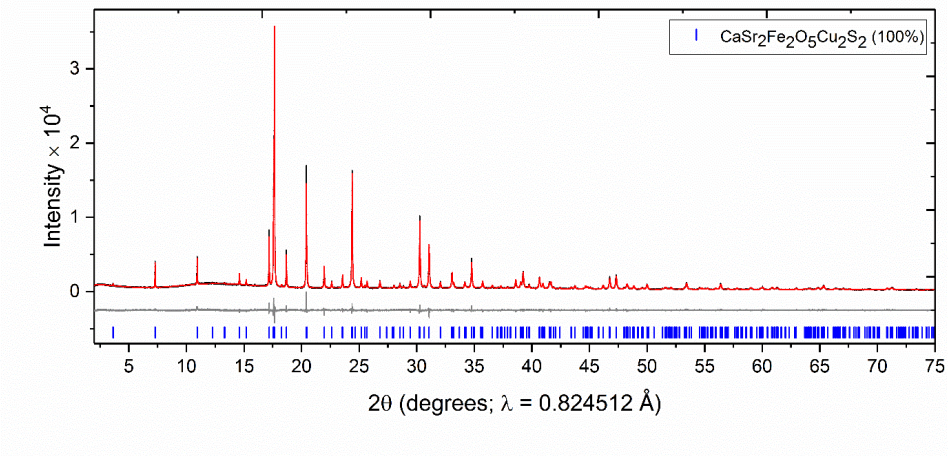

Figure S3. XRPD pattern of $CaSr_2Fe_2O_5Cu_2S_2$ measured at 300 K on the MAC detector at I11 showing the observed (black), calculated (red) and difference (grey) curves. R_{wp}: 6.413%.

Table S1. Comparison of the refinement results for $Ca_2SrFe_2O_5Cu_2Se_2$ from XRPD patterns collected at 300 K using the MAC detector at I11 and NPD patterns collected at 300 K on the WISH instrument at ISIS. The refined atomic positions from both techniques are in good agreement.

$Ca_2SrFe_2O_5Cu_2Se_2$					
Atom	**Site**	***x***	***y***	***z* (XRPD)**	***z* (NPD)**
Sr(1)	2*b*	0	0	0.5	0.5
Ca(1)	2*b*	0	0	0.5	0.5
Sr(2)	4*e*	0	0	0.63581(3)	0.63548(6)
Ca(2)	4*e*	0	0	0.63581(3)	0.63548(6)
Fe	4*e*	0	0	0.07170(2)	0.07156(3)
Cu	4*d*	0	0.5	0.25	0.25
Se	4*e*	0	0	0.19043(2)	0.19039(3)
O(1)	8*g*	0	0.5	0.08117(7)	0.08146(4)
O(2)	2*a*	0	0	0	0
				(XRPD)	**(NPD)**
Space Group: *I*4/*mmm* (No 139)				*a* = 3.914006(8) Å *c* = 26.34755(9) Å	*a* = 3.91730(3) Å *c* = 26.3733(3) Å

Table S2. Site preferences for Sr^{2+} and Ca^{2+} cations on the *Ae*(1) and *Ae*(2) crystallographic sites from NPD data.

	Temperature	***Ae*(1) Occupancy (Larger Site)**	***Ae*(2) Occupancy (Smaller Site)**
$Ca_2SrFe_2O_5Cu_2Se_2$	5.7	Sr 0.78(1) Ca 0.22(1)	Sr 0.11(1) Ca 0.89(1)
$CaSr_2Fe_2O_5Cu_2Se_2$	5.6	Sr 0.87(1) Ca 0.13(1)	Sr 0.57(1) Ca 0.43(1)
$Ca_2SrFe_2O_5Cu_2S_2$	5	Sr 0.78(1) Ca 0.22(1)	Sr 0.11(1) Ca 0.89(1)
$CaSr_2Fe_2O_5Cu_2S_2$	1.5	Sr 0.98(1) Ca 0.02(1)	Sr 0.51(1) Ca 0.49(1)

Data collected at base temperatures on the WISH instrument at ISIS. The two lowest angle (lowest resolution) banks of data were omitted from these refinements as they were dominated by magnetic Bragg peaks. These results show the same trend as that obtained by the refined occupancies from the XRPD data where there is a larger contrast between the scattering of Ca and Sr.

Table S3. Structural refinement results from room temperature XRPD data and base temperature NPD data.

	$Ca_2SrFe_2O_5Cu_2Se_2$	
	X-ray (I11) T = 300 K	Neutron (WISH) T = 5.7 K
R_{wp} (%)	7.625	4.893
a (Å)	3.914006(8)	3.90769(4)
c (Å)	26.34755(9)	26.2678(4)
V (Å^3)	403.630(2)	401.112(9)
z(*Ae*1)	0.5	0.5
z(*Ae*2)	0.63581(3)	0.63644(7)
z(Fe)	0.07170(2)	0.07167(3)
z(Cu)	0.25	0.25
z(Se)	0.19043(2)	0.19044(4)
z(O1)	0.08117(7)	0.08171(5)
z(O2)	0	0
U_{iso}(*Ae*1) (Å^2)	0.0274(2)	-
U_{iso} (*Ae*2) (Å^2)	0.0217(2)	-
U_{iso} (Fe) (Å^2)	0.0197(2)	-
U_{iso} (Cu) (Å^2)	0.0329(2)	-
U_{iso} (Se) (Å^2)	0.0231(1)	-
U_{iso} (O1) (Å^2)	0.0216(5)	-
U_{iso} (O2) (Å^2)	0.0275(11)	-
U_{11}(*Ae*)=U_{22}(*Ae*) (Å^2)	-	0.0045(5)
U_{33}(*Ae*) (Å^2)	-	0.0015(9)
U_{11}(Fe)= U_{22}(Fe) (Å^2)	-	0.0016(3)
U_{33}(Fe) (Å^2)	-	0.0051(9)
U_{11}(Cu)= U_{22}(Cu) (Å^2)	-	0.0026(7)
U_{33}(Cu) (Å^2)	-	0.0120(8)
U_{11}(Se)= U_{22}(Se) (Å^2)	-	0.0068(7)
U_{33}(Se) (Å^2)	-	0.0008(9)
U_{11}(O1) (Å^2)	-	0.0037(7)
U_{22}(O1) (Å^2)	-	0.0072(7)
U_{33}(O1) (Å^2)	-	0.0088(7)
U_{11}(O2)= U_{22}(O2) (Å^2)	-	0.0167(12)
U_{33}(O2) (Å^2)	-	0.0013(19)
Ae(1), 2*b*(0,0,0.5); *Ae*(2), 4*e*(0,0,*z*); Fe, 4*e*(0,0,*z*); Cu, 4*d*(0, 0.5, 0.25); Se, 4*e*(0,0,*z*); O(1), 8g(0, 0.5, *z*); O(2), 2*a* (0,0,0)		

	$CaSr_2Fe_2O_5Cu_2Se_2$	
	X-ray (I11) T = 300 K	Neutron (WISH) T = 5.6 K
R_{wp} (%)	8.970	4.359
a (Å)	3.93683(2)	3.93059(4)
c (Å)	26.6536(2)	26.5801(4)
V (Å^3)	413.094(5)	410.650(11)
z(*Ae*1)	0.5	0.5
z(*Ae*2)	0.63722(3)	0.63762(5)
z(Fe)	0.07048(3)	0.07053(3)
z(Cu)	0.25	0.25
z(Se)	0.19146(2)	0.19151(4)
z(O1)	0.07990(9)	0.08040(4)
z(O2)	0	0
U_{iso}(*Ae*1) (Å^2)	0.0280(3)	-
U_{iso} (*Ae*2) (Å^2)	0.0256(3)	-
U_{iso} (Fe) (Å^2)	0.0196(2)	-
U_{iso} (Cu) (Å^2)	0.0364(2)	-
U_{iso} (Se) (Å^2)	0.0238(2)	-
U_{iso} (O1) (Å^2)	0.0187(6)	-
U_{iso} (O2) (Å^2)	0.0260(14)	-
U_{11}(*Ae*)=U_{22}(*Ae*) (Å^2)	-	0.0068(4)
U_{33}(*Ae*) (Å^2)	-	0.0054(8)
U_{11}(Fe)= U_{22}(Fe) (Å^2)	-	0.0000(3)
U_{33}(Fe) (Å^2)	-	0.0074(9)
U_{11}(Cu)= U_{22}(Cu) (Å^2)	-	0.0010(6)
U_{33}(Cu) (Å^2)	-	0.0141(8)
U_{11}(Se)= U_{22}(Se) (Å^2)	-	0.0014(6)
U_{33}(Se) (Å^2)	-	0.0071(9)
U_{11}(O1) (Å^2)	-	0.0034(7)
U_{22}(O1) (Å^2)	-	0.0078(6)
U_{33}(O1) (Å^2)	-	0.0106(7)
U_{11}(O2)= U_{22}(O2) (Å^2)	-	0.0078(10)
U_{33}(O2) (Å^2)	-	0.0010(17)
Ae(1), 2*b*(0,0,0.5); *Ae*(2), 4*e*(0,0,*z*); Fe, 4*e*(0,0,*z*); Cu, 4*d*(0, 0.5, 0.25); Se, 4*e*(0,0,*z*); O(1), 8g(0, 0.5, *z*); O(2), 2*a* (0,0,0)		

	$Ca_2SrFe_2O_5Cu_2S_2$	
	X-ray (I11) T = 300 K	Neutron (WISH) T = 5 K
R_{wp} (%)	7.076	4.551
a (Å)	3.88060(2)	3.87518(4)
c (Å)	25.6025(1)	25.5230(4)
V (Å^3)	385.550(4)	383.279(11)
z(*Ae*1)	0.5	0.5
z(*Ae*2)	0.64048(3)	0.64110(8)
z(Fe)	0.07406(2)	0.07397(4)
z(Cu)	0.25	0.25
z(S)	0.19315(3)	0.19286(11)
z(O1)	0.08413(6)	0.08460(5)
z(O2)	0	0
U_{iso}(*Ae*1) (Å^2)	0.0171(2)	-
U_{iso} (*Ae*2) (Å^2)	0.0132(2)	-
U_{iso} (Fe) (Å^2)	0.0102(1)	-
U_{iso} (Cu) (Å^2)	0.0239(1)	-
U_{iso} (S) (Å^2)	0.0135(2)	-
U_{iso} (O1) (Å^2)	0.0158(4)	-
U_{iso} (O2) (Å^2)	0.0178(9)	-
U_{11}(*Ae*)=U_{22}(*Ae*) (Å^2)	-	0.0080(5)
U_{33}(*Ae*) (Å^2)	-	0.0011(11)
U_{11}(Fe)= U_{22}(Fe) (Å^2)	-	0.0025(3)
U_{33}(Fe) (Å^2)	-	0.0070(9)
U_{11}(Cu)= U_{22}(Cu) (Å^2)	-	0.0018(6)
U_{33}(Cu) (Å^2)	-	0.0114(8)
U_{11}(S)= U_{22}(S) (Å^2)	-	0.0000(14)
U_{33}(S) (Å^2)	-	0.0000(20)
U_{11}(O1) (Å^2)	-	0.0035(7)
U_{22}(O1) (Å^2)	-	0.0083(6)
U_{33}(O1) (Å^2)	-	0.0094(7)
U_{11}(O2)= U_{22}(O2) (Å^2)	-	0.0241(12)
U_{33}(O2) (Å^2)	-	0.0000(17)
Ae(1), 2*b*(0,0,0.5); *Ae*(2), 4*e*(0,0,*z*); Fe, 4*e*(0,0,*z*); Cu, 4*d*(0, 0.5, 0.25); S, 4*e*(0,0,*z*); O(1), 8g(0, 0.5, *z*); O(2), 2*a* (0,0,0)		

	$CaSr_2Fe_2O_5Cu_2S_2$	
	X-ray (I11) T = 300 K	Neutron (WISH) T = 1.5 K
R_{wp} (%)	6.380	4.378
a (Å)	3.90253(2)	3.89682(5)
c (Å)	25.9609(1)	25.8825(5)
V (Å^3)	395.379(4)	383.279(11)
z(*Ae*1)	0.5	0.5
z(*Ae*2)	0.64162(2)	0.64196(6)
z(Fe)	0.07273(2)	0.07262(4)
z(Cu)	0.25	0.25
z(S)	0.19425(3)	0.19411(10)
z(O1)	0.08253(5)	0.08335(5)
z(O2)	0	0
U_{iso}(*Ae*1) (Å^2)	0.0162(2)	-
U_{iso} (*Ae*2) (Å^2)	0.0133(2)	-
U_{iso} (Fe) (Å^2)	0.0100(1)	-
U_{iso} (Cu) (Å^2)	0.0251(1)	-
U_{iso} (S) (Å^2)	0.0112(2)	-
U_{iso} (O1) (Å^2)	0.0159(4)	-
U_{iso} (O2) (Å^2)	0.0137(8)	-
U_{11}(*Ae*)=U_{22}(*Ae*) (Å^2)	-	0.0057(4)
U_{33}(*Ae*) (Å^2)	-	0.0000(10)
U_{11}(Fe)= U_{22}(Fe) (Å^2)	-	0.0007(3)
U_{33}(Fe) (Å^2)	-	0.0070(10)
U_{11}(Cu)= U_{22}(Cu) (Å^2)	-	0.0000(5)
U_{33}(Cu) (Å^2)	-	0.0121(7)
U_{11}(S)= U_{22}(S) (Å^2)	-	0.0000(14)
U_{33}(S) (Å^2)	-	0.0000(19)
U_{11}(O1) (Å^2)	-	0.0042(7)
U_{22}(O1) (Å^2)	-	0.0059(6)
U_{33}(O1) (Å^2)	-	0.0070(6)
U_{11}(O2)= U_{22}(O2) (Å^2)	-	0.0148(10)
U_{33}(O2) (Å^2)	-	0.0000(15)
Ae(1), 2*b*(0,0,0.5); *Ae*(2), 4*e*(0,0,*z*); Fe, 4*e*(0,0,*z*); Cu, 4*d*(0, 0.5, 0.25); S, 4*e*(0,0,*z*); O(1), 8g(0, 0.5, *z*); O(2), 2*a* (0,0,0)		

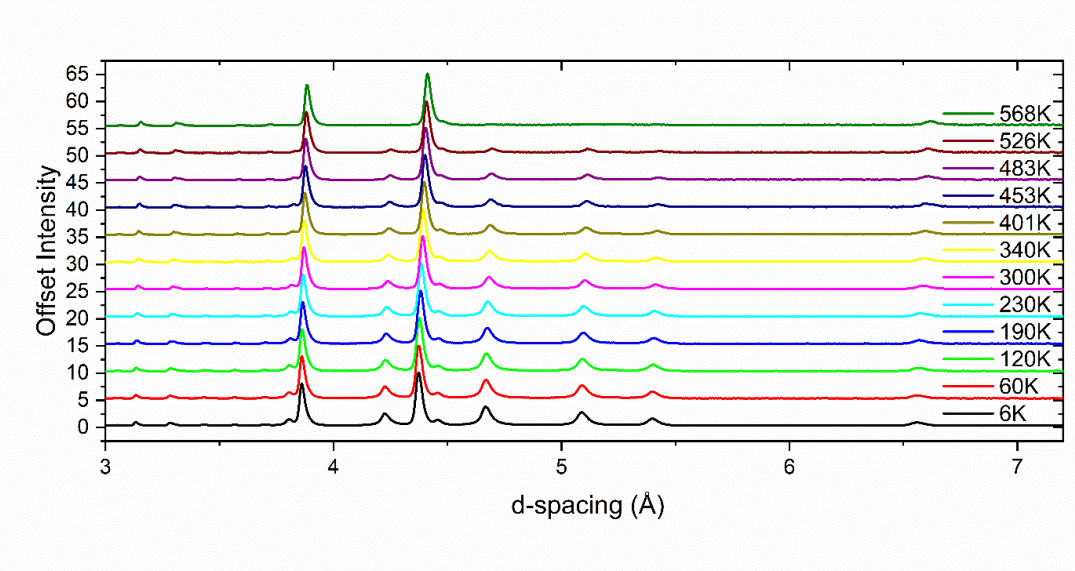

Figure S4. NPD patterns of $Ca_2SrFe_2O_5Cu_2Se_2$ (combination of banks 3 and 8 with average $2\theta = 90°$) at different temperatures measured on the WISH instrument at ISIS showing the evolution of the magnetic peaks. Magnetic Bragg peaks were still present at 526 K before disappearing by 568 K.

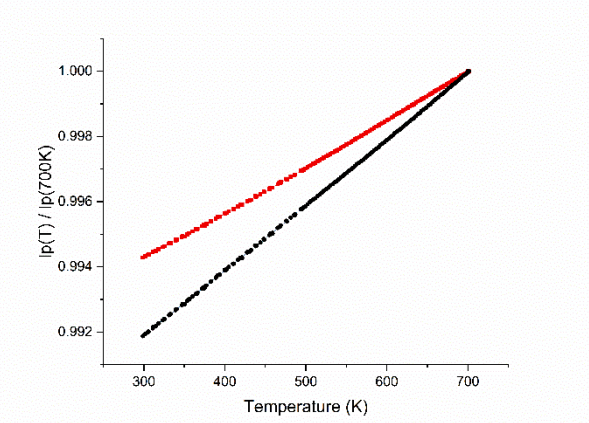

Figure S5. Lattice parameters (lp) *a* (red) and *c* (black) of $Ca_2SrFe_2O_5Cu_2Se_2$ at temperatures between 300 K and 700 K, normalised against their values at 700 K. Lattice parameter values have been refined from XRPD patterns collected at each temperature using the PSD at I11. There are no signs of any structural distortions.

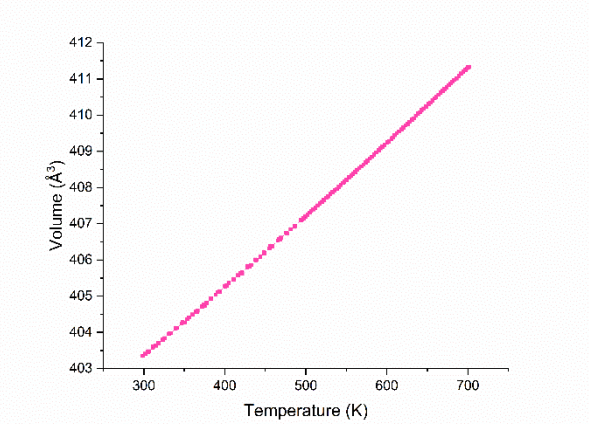

Figure S6. Unit cell volume of $Ca_2SrFe_2O_5Cu_2Se_2$ at temperatures between 300 K and 700 K, normalised against the value at 700 K. Unit cell volume values have been refined from XRPD patterns collected at each temperature using the PSD at I11. There are no signs of any structural distortions.

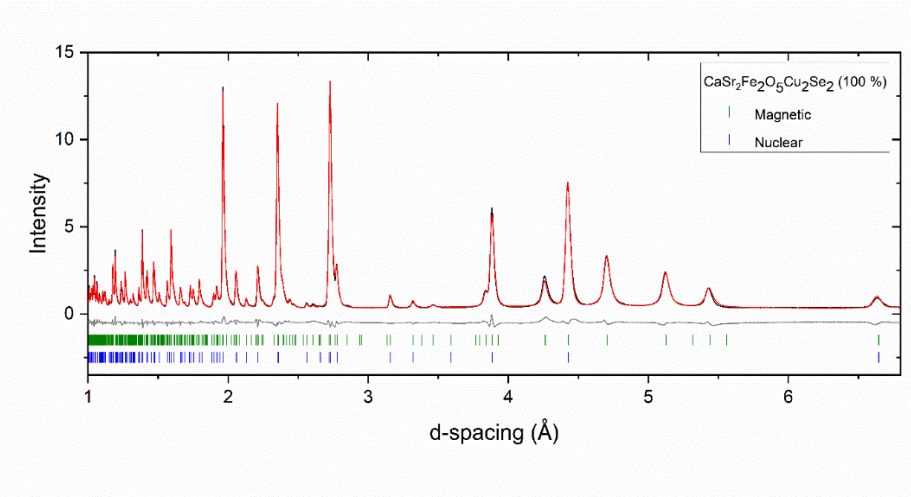

Figure S7. NPD pattern of $CaSr_2Fe_2O_5Cu_2Se_2$ (combination of banks 3 and 8 with average $2\theta = 90°$) measured at 5.6 K on the WISH instrument at ISIS showing the observed (black), calculated (red) and difference (grey) curves. R_{wp}: 4.585%.

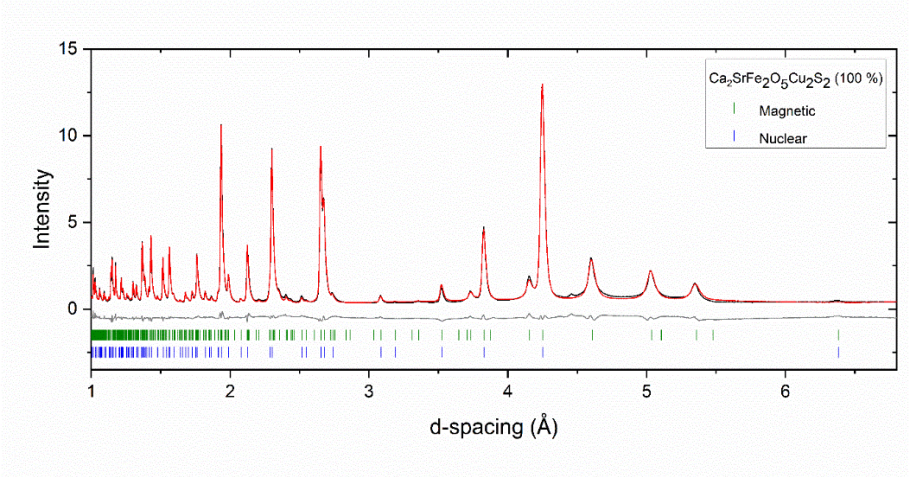

Figure S8. NPD pattern of $Ca_2SrFe_2O_5Cu_2S_2$ (combination of banks 3 and 8 with average $2\theta = 90°$) measured at 5 K on the WISH instrument at ISIS showing the observed (black), calculated (red) and difference (grey) curves. R_{wp}: 5.016%.

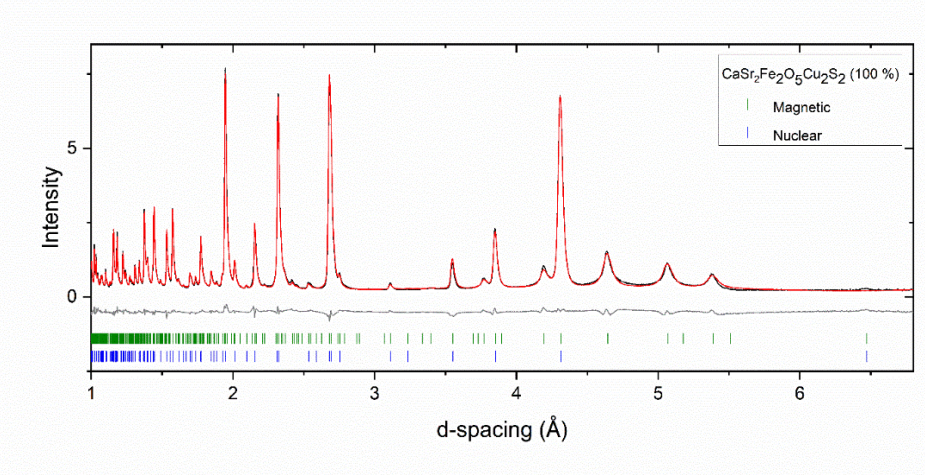

Figure S9. NPD pattern of $CaSr_2Fe_2O_5Cu_2S_2$ (combination of banks 3 and 8 with average $2\theta = 90°$) measured at 1.5 K on the WISH instrument at ISIS showing the observed (black), calculated (red) and difference (grey) curves. R_{wp}: 4.986%.

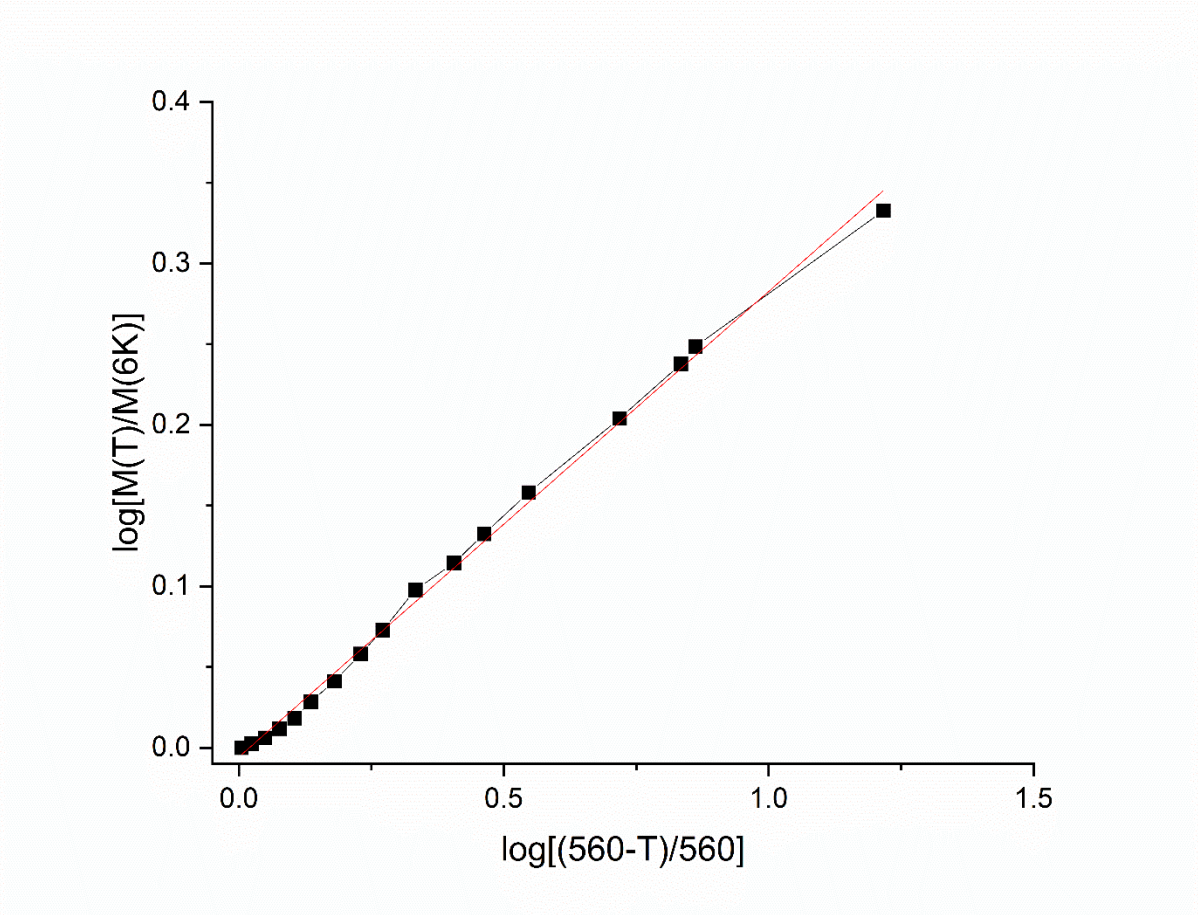

Figure S10. Plot to determine the critical exponent, β, of the $Ca_2SrFe_2O_5Cu_2Se_2$ magnetic transition using the equation $\left[\frac{M(T)}{M(Base\ T)}\right] = \left[\frac{T_N - T}{T_N}\right]^{\beta}$ where M is the magnetic moment, T_N is the Néel temperature and T is the temperature. The Néel temperature used is 560(5) K and β = 0.29(2).